Climate Dynamics (2025) 63:90
https://doi.org/10.1007/s00382-024-07577-5

ORIGINAL ARTICLE

Impact of mid-high latitude circulation and surface thermal forcing on drought events in Central Asia

Yu Ren[1] · Haipeng Yu[2] · Jianping Huang[3] · Jie Zhou[1] · Hongyu Luo[2] · Shanling Cheng[2]

Received: 9 October 2024 / Accepted: 27 December 2024 / Published online: 16 January 2025

Abstract

With the significant warming, Central Asia (CA) has suffered from frequent drought events and vegetation degradation. However, whether it is the large-scale circulation dynamics or the surface local thermal mechanism that plays the dominant role in the drought remains unknown. Here we used 3-month Standardized Precipitation Evaporation Index in August to identify the summer drought events for 1980–2022 and conducted a composite analysis. Results indicate that the drought related wave train, originating from mid-high latitude North Atlantic (NA), has a barotropic vertical structure and propagates eastward, featuring a positive geopotential height center in CA. The pronounced warm sea surface temperature (SST) over the middle-latitude NA and cold SST over the high-latitude NA contribute to the Rossby wave formation, which is verified by an analysis of the apparent vorticity anomaly and linear baroclinic model experiments. The anticyclone anomaly over CA, corresponding to strong vertical subsidence, enhances downward shortwave radiation and surface sensible heat flux, while significantly reducing surface latent heat flux. The maintenance of drought is usually associated with persistent precipitation deficits. By using the backward moisture tracking model, we further found that the recycled precipitation, induced by the local evapotranspiration, contributes to the 88.39% reduction of total precipitation during drought periods, whereas the inflow of external advected moisture shows no significant decrease. The above results highlight the dominated role of local land–atmosphere interactions responsible for the drought through reduced local evapotranspiration, with large-scale circulation anomalies providing a conducive background for the drought.

Keywords Mid-high latitude circulation · Surface thermal forcing · Central Asia · Drought events · SST anomalies · Recycled precipitation

1 Introduction

Central Asia (CA) is located in the hinterland of the Eurasian continent, spanning from the Caspian Sea to the northwest region of China, far from the ocean, with scarce sources of moisture. The region is the "hotspot" for climate change, experiencing significant warming over the past 100 years (Ji et al. 2014; Huang et al. 2017), particularly from 1979 to 2011, with the rate accelerating to approximately 0.338 °C/10 year, which far exceeds the averages for global land (Peng et al. 2019). The increase in temperature intensifies the frequency and intensity of CA droughts (Guo et al. 2018; Jiang and Zhou 2021, 2023; IPCC 2021). Dryness characterizes arid and semi-arid regions, yet droughts represent an unexpected decrease in rainfall over a specific time, significantly affecting the region. As one of the most complicated and severe natural disasters (Portela et al. 2015), drought has severely threatened crop productivity, industry and society (Mishra and Singh 2010). For example, in early June 2021, due to record-breaking heat and insufficient rainfall, CA suffered from prolonged drought. More than 2000 domesticated animals died due to a lack of water and forage, leading to increased food prices (Jiang and

✉ Haipeng Yu
yuhp@lzb.ac.cn

1 College of Atmospheric Sciences, Lanzhou University, Lanzhou 730000, China

2 State Key Laboratory of Cryospheric Science and Frozen Soil Engineering, Nagqu Plateau Climate and Environment Observation and Research Station of Tibet Autonomous Region, Northwest Institute of Eco-Environment and Resources, Chinese Academy of Sciences, Lanzhou 730000, China

3 Collaborative Innovation Center for Western Ecological Safety, Lanzhou University, Lanzhou 730000, China

Zhou 2023). In the arid and semi-arid regions, coupled with the frequent occurrence of drought events, this leads to a series of problems such as intensified contradiction between water supply–demand, increased desertification, and more frequent sandstorms, further exacerbating the already fragile ecological environment of CA (Bestelmeyer et al. 2015; Li et al. 2015; Chen et al. 2016; Zhang et al. 2018). Therefore, in light of the severe situation of frequent droughts in CA in recent years, understanding the underlying physical mechanisms of drought events over CA is urgent and of significant practical importance, as it helps meet the needs for the rational utilization of water resources and maintain ecological security and sustainable development, especially in drylands.

Previous studies have documented that various large-scale teleconnection patterns affect wet/dry conditions by modulating precipitation in CA. On the interdecadal scale, since the 1990s, the Interdecadal Pacific Oscillation (IPO) has undergone a phase shift from positive to negative, leading to reduced spring precipitation and exacerbating the decrease in soil moisture at the start of the growing season over CA (Jiang and Zhou 2023). The positive phase of Atlantic Multidecadal Oscillation (AMO) in the twenty-first century corresponds to the weakened westerly and less CA precipitation (Guo et al. 2022). While the negative east Atlantic/western Russia pattern can lead to the cooling of the upper troposphere and the formation of an anomalous cyclone over CA, inducing precipitation in CA (Ma et al. 2020; Ren and Zhao 2023). On the interannual scale, the El Nino–Southern Oscillation significantly influences summer CA precipitation by adjusting the strength and location of the westerly jet stream (Hu et al. 2017). When the Indian Ocean sea surface temperature (SST) is cooler, the South Asian summer monsoon intensifies, and the North Indian continent has a positive heat source anomaly; this condition corresponds to a northward shift of the subtropical westerly jet, resulting in sinking motions and reduced rainfall over southeastern CA (Meng et al. 2021; Wei et al. 2023). The Indian summer monsoon and Tibetan Plateau heating, both affected by south Indian Ocean Dipole in February, have synergistic impact the interannual variation of summer CA precipitation (Zhao et al. 2022). Additionally, Bothe et al. (2012) indicate that the North Atlantic (NA) SST anomaly also influences the extreme and severe dryness over CA. However, it still lacks a clear analytical framework for determining which locations trigger the teleconnection wave trains that dominate the maintenance of drought events in CA on an interannual scale.

Anomalies in large-scale circulation systems create the dynamic conditions for drought persistence and are often accompanied by changes in moisture transport and local evapotranspiration. These moisture transport anomalies are directly linked to precipitation anomalies, such as drought and flood. Therefore, understanding moisture changes for drought is crucial. Previous studies have indicated that the spring drying trend in southeastern CA is mainly caused by reduced local evaporation and weakened moisture transport from the Arabian Peninsula and Arabian Sea. The summer drying trend in northern Central Asia can be attributed to decreased local evaporation and reduced moisture transport from Scandinavia (Jiang et al. 2020). The dry season of CA shows a reduction in net moisture inflow, primarily due to decreased water vapor from central and western Eurasia, which leads to a decrease in precipitation minus evapotranspiration (P − E) (Ren et al. 2022). Additionally, the local thermodynamic mechanism plays a critical role in maintaining and intensifying droughts by influencing the temperature and local evaporation. Drought events often coincide with anomalous subsidence and moisture flux divergence, leading to reduced cloud cover and increased downward shortwave radiation; the adiabatic warming effect of subsidence intensifies surface air heating, further favoring drought occurrence (Zhou et al. 2024). Warming increases atmospheric moisture demand; initially, actual evapotranspiration briefly spikes anomalously (Zhao et al. 2023), but as water supply is limited in arid regions, soil moisture quickly depletes, causing latent heat flux to decrease and sensible heat flux to increase. This reduction in local actual evapotranspiration then causes a decrease in recycled and total precipitation, intensifying drought through a local coupled soil-temperature process (Mukherjee et al. 2018). Quantifying changes in moisture transport process, precipitation recycling and water balance during drought periods can deepen our understanding of atmospheric water cycle and is beneficial for forecasting drought extreme event (Roy et al. 2019; Guan et al. 2022). However, current research on the quantitative analysis of the relative contributions of local evapotranspiration (affected by local thermodynamic mechanisms) and external moisture advection (affected by large-scale circulation dynamics) to drought events in CA is extremely scarce.

Therefore, in this study, we focus on summer drought events across CA, identifying the main atmospheric circulation patterns associated with drought events and extracting the related teleconnection wave trains at the interannual scale. The study further investigates the mechanisms of how the wave train develops and examines whether the wave train is excited by thermal anomaly of underlying surface. In addition, a backward moisture trajectory tracking model is used to quantify the relative contributions of external moisture transport anomalies and local actual evapotranspiration anomalies to the drought events over CA. Through the above exploration, we aim to provide a comprehensive analysis of the physical causes underlying drought events.

The structure of this paper is organized as follows. Section 2 provides a detailed description of the datasets and methods used in the study. Section 3 identifies the drought events and examines the associated circulation anomaly. Section 4 investigates the dynamics of the teleconnection wave train in detail. Section 5 quantifies the contributions of external moisture advection and local evapotranspiration to the drought events. Section 6 conducts the model experiment to validate the role of thermal anomaly of underlying surface. Section 7 offers the summary and discussion.

2 Data sets and methods

2.1 Data

The drought measurement is complex with no uniform standard (Heim 2002). Various drought indices have been used to examine changes in the wet-dry conditions of CA, such as the standardized precipitation index (SPI, McKee et al. 1995), Palmer Drought Severity Index (PDSI, Palmer 1965; Li et al. 2017), and standardized precipitation evaporation index (SPEI, Vicente-Serrano et al. 2010). The PDSI has a fixed time scale, and its accuracy largely depends on the quality of soil moisture data (Kumar et al. 2013). Compared to the SPI index, the SPEI index accounts for temperature anomalies in addition to precipitation deficits. Therefore, using the SPEI index can more reasonably identify drought events in CA. Considering that summer precipitation is closely related to annual precipitation and significantly affects the annual precipitation variability in CA (Hu et al. 2017), coupled with the fact that droughts are often accompanied by severe precipitation deficits, we therefore focus our research on interannual variations of summer droughts. The SPEI-3 in August serves as an effective indicator of summer drought. The data for SPEI-3 is sourced from the Climate Research Unit (CRU) Version 4.08, spanning from 1901 to 2022 with a spatial resolution of 0.5°×0.5°.

The monthly geopotential height, winds, radiative flux, cloud cover, surface and air temperature, along with 6-h mean winds, precipitation, evaporation and precipitable water are derived from the Modern-Era Retrospective Analysis for Research and Applications, version 2 (MERRA-2) with a resolution of 0.625°×1.25°, which is available from 1980 to present (Gelaro et al. 2017). Besides, we also obtained the monthly mean extended reconstructed SST version 5 (ERSST v5), which spans from 1854 to present with a horizontal resolution of 2°×2°.

2.2 Methods

2.2.1 The precipitation dynamic recycling model (DRM)

To understand the contribution of the recycling process to precipitation deficit, we conducted the DRM to calculate the recycling ratio, which is derived from the atmospheric moisture balance equation (Eq. (1); Dominguez et al. 2006). The model has been used for exploring precipitation recycling and tracing moisture source (Dominguez and Kumar 2008; Pathak et al. 2014; Hua et al. 2017a, b; Ren et al. 2022).

$$\frac{\partial W}{\partial \mathrm{t}} + \frac{\partial Wu}{\partial x} + \frac{\partial Wv}{\partial \mathrm{y}} = E - P + res \tag{1}$$

The u and v represents moisture that weighted zonal and meridional winds, the specific calculating process can be seen in Table 1. The W, E and P represent the precipitable water, evapotranspiration and precipitation, respectively. The W has two sources: the external advected moisture and local evapotranspiration. The model assumes that the water vapor from evapotranspiration and advection is well mixed in the vertical direction. Therefore, the mass conservation equation can be expressed as follows:

$$W\frac{\partial \rho}{\partial t} + Wu\frac{\partial \rho}{\partial x} + Wv\frac{\partial \rho}{\partial y} = E(1-\rho) \tag{2}$$

where ρ is the recycling ratio, and $\rho = \frac{P_m}{P} = \frac{W_m}{W}$. The subscript m represents recycled components. By solving the above differential equation, we can obtain the expression for recycling ratio in one cell as follows:

$$\rho(\mathrm{s}) = 1 - \exp\left[-\int_{s_0}^{s}\left(\frac{E}{W}\right)ds\right] \tag{3}$$

where s is the moisture trajectory, and s_0 represents the starting point of the moisture trajectory. Further we can calculate the region recycling ratio for a region including z grid cells, the specific formula can be seen in Table 1.

Table 1 The derived variables from the $\overline{q}$, $\widehat{\overline{u}}$, $\widehat{\overline{v}}$, q', $\widehat{u'}$, and $\widehat{v'}$, where are the mean and transient values for the specific humidity and zonal and meridional wind, respectively

Abbreviation	Variable description	Equation
u	The moisture-weighted vertically integrated zonal winds	$u = \int_0^{P_0}\overline{q}\widehat{\overline{u}}dp + \int_0^{P_0}\overline{q'\widehat{u'}}dp$
v	The moisture-weighted vertically integrated meridional winds	$v = \int_0^{P_0}\overline{q}\widehat{\overline{v}}dp + \int_0^{P_0}\overline{q'\widehat{v'}}dp$
R_z	The regional precipitation recycling ratio	$\rho = \frac{P_m}{P} = \frac{\sum_{i=1}^{z}\rho_i P_i \Delta A_i}{\sum_{i=1}^{z}P_i\Delta A_i}$

A represented the area of the cell

2.2.2 Moisture source detection

To accurately quantify the contribution of moisture sources to precipitation in CA, we employed the 'moisture source detection' method developed by Sodemann et al. (2008), which tracks the changes in specific humidity of an air parcel along its trajectory from the source to the target area. This method considers the temporal sequence of evaporation into and precipitation from the air parcel. It has been widely applied in previous studies (e.g., Peng et al. 2020; Ren et al. 2022; Zhang et al. 2022). However, since DRM is a two-dimensional model, we primarily used the variable W, rather than specific humidity, to calculate moisture changes within the air column during backward tracking, where multiple processes of moisture absorption and release occur. Our adaptation of the Sodemann method involves the following three steps:

(i) Drawing on the results of DRM, we selected all trajectories bound for the target area that exhibit moisture release within that region.

(ii) As these trajectories go forward from their moisture uptake locations to the target area, the moisture content in the whole air column can fluctuate due to multiple processes of evaporation and precipitation. To calculate the changes, we calculate $\Delta W = W(t) - W(t-6h)$ for the kth backward trajectory over time t. The first point where $\Delta W > 0$ is marked as the starting point for tracking. At locations where ΔW is positive, evapotranspiration contributes moisture content to the entire air column. The fractional contribution (f_n) of ΔW to the moisture in a unit area air column (W_n) at that specific moment n, is determined as follows:

$$f_n^k = \frac{\Delta W_n^k}{W_n^k} \tag{4}$$

As the air column moves towards the target area, it engages in multiple cycles of absorbing and releasing water vapor. New instances of moisture uptake can reduce the relative contribution of earlier uptakes. Therefore, to accurately account for these dynamics, the contributions of moisture from previous time m must be recalibrated as follows:

$$f_m^k = \frac{\Delta W_m^k}{W_n^k}, m < n \tag{5}$$

where f_m represents the fractional contributions of all moisture uptakes at earlier times m relative to the new moisture at moment n. When $\Delta W < 0$, precipitation results in the release of moisture across the entire air column at that location, thus diminishing the influence of all prior contributions of ΔW to the moisture in a unit area air column. Consequently, all previous contributions to the moisture of the entire air column are proportionally adjusted in response to the precipitation, which is discounted as follows:

$$\Delta W_m^{k'} = \Delta W_m^k + \Delta W_n^k \Delta f_m^k \quad \text{for all } m < n \tag{6}$$

When the air column arrives at the target region, the cumulative sum of the most recent fractional contributions from all uptake points reflects the total contribution from all points along the trajectory throughout the entire period.

(iii) The contribution percentage of the jth moisture source region to CA precipitation is calculated as:

$$CP_j = \frac{\sum_{k=1}^{ktot} \Delta W^k(j)}{\sum_{k=1}^{ktot} W_{t=-6h}} \times 100\% \tag{7}$$

where CP is the sum of the contributions of all trajectories for the jth moisture source region.

2.2.3 The linear baroclinic model (LBM)

The LBM model (Watanabe and Kimoto 2000) is a dry atmospheric model developed to simulate the atmosphere dynamic responses to idealized forcing such as diabatic heating and convergence. For our simulations, we used the T42L20 version of the LBM, which incorporates a T42 horizontal resolution and 20 sigma levels. The model's background state is based on the climatological mean of summer derived from the NCEP/NCAR reanalysis for the period 1958–1997. To ensure a stable response to heating forcing, the model is integrated over a period of 60 days. We focused on averages from days 30 to 60 to characterize the linear response of atmospheric circulation, analyzing variables such as meridional wind and geopotential height.

2.2.4 Other methods

The Empirical Orthogonal Function (EOF; Lorenz 1956) analysis is utilized to extract the dominant spatial mode of the August SPEI-3 index over CA. To emphasize interannual variability, a 9-year sliding average is removed from all variables. Additionally, composite analysis and regression are performed, with statistical significance assessed using the Student's t-test.

The wave activity flux (WAF; unit: $m^2 s^{-2}$), as introduced by Takaya and Nakamura, is calculated to elucidate the propagation of anomalous Rossby waves across the mid-to-high latitudes of the Northern Hemisphere. Its expression is as follows:

$$WAF = \frac{pcos\varphi}{2\left|\overline{U}\right|}\begin{bmatrix} \frac{\overline{U}}{a^2cos^2\varphi}(\psi'^2_x - \psi'\psi_{xx}) + \frac{\overline{v}}{a^2cos^2\varphi}(\psi_x\psi'_y - \psi'\psi_{xy}) \\ \frac{\overline{U}}{a^2cos\varphi}(\psi'_x\psi'_y - \psi'\psi'_{xy}) + \frac{\overline{v}}{a^2}(\psi'^2_y - \psi'\psi_{yy}) \end{bmatrix} \tag{8}$$

where ψ denotes the geostrophic stream function, φ is the latitude, p is the pressure, a is the earth's radius, and u and v are the zonal and meridional winds. The subscripts y and x indicate the partial differential in latitudinal and meridional directions, respectively. The overbar and prime represent the climatology (1980–2022) and anomalies during drought periods, respectively.

The wave train is sustained primarily through two mechanisms of energy extraction from the mean flow: the conversion of kinetic energy (CK) and the conversion of available potential energy (CP). These conversions are quantified using the methods outlined by Kosaka and Nakamura (2006):

$$CK = \frac{v'^2 - u'^2}{2}\left(\frac{\partial\overline{u}}{\partial x} - \frac{\partial\overline{v}}{\partial y}\right) - u'v'\left(\frac{\partial\overline{u}}{\partial y} + \frac{\partial\overline{v}}{\partial x}\right) \tag{9}$$

$$CP = -\frac{f}{\sigma}\left(v'T'\frac{\partial\overline{u}}{\partial p} - u'T'\frac{\partial\overline{v}}{\partial p}\right) \tag{10}$$

where the positive CK(CP) means the anomalies extracted the kinetic energy (available potential energy) from the mean flow.

Following Kosaka and Nakamura (2006), the linearized vorticity equation can be expressed as:

$$RWS \underbrace{-\overline{u}_\psi\frac{\partial\zeta'}{\partial \boldsymbol{x}}}_{ZA} \underbrace{-\overline{v}_\psi\frac{\partial\zeta'}{\partial \boldsymbol{y}}}_{MA} \underbrace{-u'_\psi\frac{\partial\overline{\zeta}}{\partial \boldsymbol{x}}}_{\beta\_x} \underbrace{-v'_\psi\frac{\partial\left(f+\overline{\zeta}\right)}{\partial \boldsymbol{y}}}_{\beta\_y} -Res = 0 \tag{11}$$

where $V_\psi = (u_\psi, v_\psi)$ denotes rotational wind components, and ζ is the relative vorticity. The terms of ZA and MA indicate the advections of anomalous vorticity due to climatological mean rotational zonal and meridional winds, respectively. The β term denotes the horizontal advection of the mean vorticity by anomalous winds. The Res term includes the contribution of vertical advection, nonlinear effects, and dissipation. A positive value of each term in Eq. (11) represents a positive cyclonic vorticity tendency. RWS denotes the linearized barotropic Rossby wave source, which can be calculated referring to Sardeshmukh and Hoskins (1988):

$$RWS = \underbrace{-\left(f+\overline{\zeta}\right)\nabla_H\cdot V'_\chi}_{S1} \underbrace{-\zeta'\nabla_H\cdot\overline{V_\chi}}_{S2} \underbrace{-V'_\chi\cdot\nabla_H\left(f+\overline{\zeta}\right)}_{S3} \underbrace{-\overline{V_\chi}\cdot\nabla_H\zeta'}_{S4} \tag{12}$$

where $V_\chi = (u_\chi, v_\chi)$ represent divergent wind components. The sum of $S1$ and $S2$ on the right-hand side of Eq. (12) is the vortex stretching term induced by the product of anomalous divergence and climatological absolute vorticity, and arising from the interaction between climatological divergence and anomalous vorticity, respectively. The sum of $S3$ and $S4$ is the vorticity advection term. The $S3$ term represents the advection of climatological mean absolute vorticity by anomalous divergence flow, and $S4$ is the advection of anomalous absolute vorticity by climatological mean divergence flow (Lu and Kim 2004).

3 Identification of summer drought and associated circulation anomaly

The time series of the area-averaged summer precipitation in CA and August SPEI-3 demonstrate high consistency in their fluctuations, with significant year-to-year variations (Fig. 1a). However, their trends diverge: the former shows an increasing trend, while the latter reveals a decreasing trend. This discrepancy arises because SPEI accounts not only for precipitation but also incorporates the effects of significant warming, which results in a drying trend. In order to examine the spatiotemporal characteristics of CA drought, we first performed the EOF analysis to the August SPEI-3 during 1980–2022. The EOF1 mode of SPEI-3 accounts for 39.8% of the total variance and exhibits a largely consistent spatial pattern across CA, except for northeastern subregions (Fig. 1b). The first principal component (PC1) of EOF1 features pronounced interannual variability and is highly correlated with the SPEI-3 index, showing a correlation coefficient of 0.73. we defined a drought year as any year in which PC1 is less than -1. Accordingly, the years 1984, 1995, 1997, 2006, 2008, and 2014 are identified as drought years (Fig. 1c) and are selected as composites to represent the drought periods.

The atmospheric circulation anomalies provide the background for the drought. The composite analysis of 250 hPa geopotential height shows a "+ − +" structure, with an anomalous high-pressure system is observed over the CA (Fig. 2a). At 850 hPa, the spatial pattern of geopotential height anomalies is similar with that at 250 hPa, which indicates this is an equivalent barotropic structure from the lower-troposphere to upper-troposphere (Fig. 2b). The wave activity fluxes are shown to estimate the Rossby wave propagation associated with CA drought (Fig. 2c). Wave energy originates from the high latitudes of the NA, intensifies over Europe, passes through the Mediterranean and Aral Sea, and then turns eastward towards CA. Correspondingly, the meridional wind is characterized by an alternating northerly and southerly anomalies within

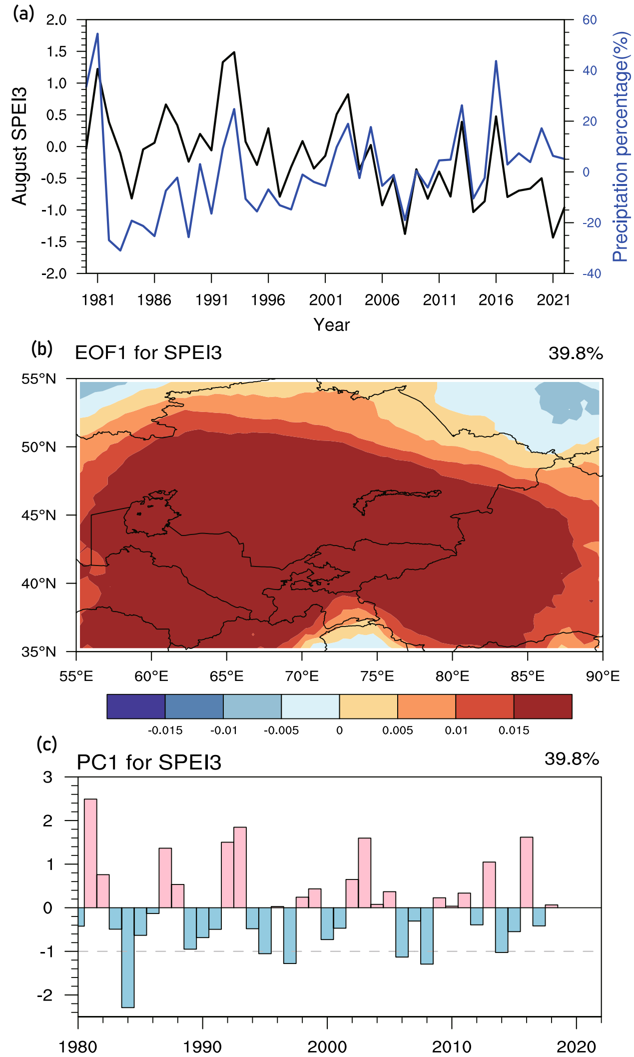

Fig. 1 **a** The time series of August SPEI-3 (black line) and the summer precipitation anomalies (blue line) averaged over CA. **b** The spatial pattern of the EOF1 mode for interannual variation (removing the 9-year sliding average) of August SPEI-3 over CA. **c** The normalized PC1 time series

the Rossby wave train (Fig. 2c). The Fig. 2d gives the vertical structure of the composited geopotential height, vertical velocity and temperature anomalies along the major centers labeled A, B, C, and D in Fig. 2a, which confirms the quasi-barotropic structure of the atmospheric wave train. The anti-cyclonic and positive temperature center in CA is the strongest among these three action centers, with the profound descending motion controlling the CA (Fig. 2d). In addition, the strongest temperature anomalies over CA are located in the upper layer (i.e. 300 hPa) of the troposphere, and temperature in the North Atlantic shows a positive anomaly below 300 hPa while a negative anomaly above 300 hPa (Fig. 2d).

4 Large-scale dynamics mechanisms responsible for the CA drought

We have presented the circulation pattern and suggested that the wave train originates from high latitude NA, influencing drought conditions over CA. However, the mechanisms triggering and maintaining the wave train remain to be elucidated. By conducting an analysis of the linearized vorticity budget, the formation and persistence of the wave train can be further determined. Figure 3a–f illustrates the spatial distribution of each term at 250 hPa in the linearized vorticity equation (Eq. (11)). In the upper troposphere, a strong anticyclonic vorticity source is found around 65°N, 30°W. The positive and negative wave sources alternate along the atmospheric wave train, with largest anticyclonic vorticity source observed in east of CA (Fig. 3a). The contributions of the *ZA* (Fig. 3b) and β_y term (Fig. 3e) are significantly stronger than the others, and they exhibit opposite signs. This pattern suggests that the advection of disturbance vorticity by the mean zonal rotating wind is largely offset by the β effect, confirming that the wave train is indeed a stationary Rossby wave. The contributions of β_x and *MA* term (Fig. 3c, d) to the teleconnection are weak, and the residual term is dispersed and small in amplitude (Fig. 3f).

Further exploring which process plays a pivotal role in the generation of Rossby wave, we divided the anomalous *RWS* int two components: the vortex stretching term and vorticity advection term. The distribution of the vortex stretching term is highly consistent with the total *RWS* in both spatial pattern and values (Figs. 3a, 4a), indicating a close relationship between *RWS* and convergence and divergence in the upper troposphere, while the contributions of the vorticity advection term are relatively weak (Fig. 4b).

To clarify which energy source maintaining this atmospheric wave train, we examined the baroclinic and barotropic energy conversions processes during the drought periods. Figure 5a, b exhibits the spatial pattern of *CK* and *CP* integrated from 1000 to 100 hPa. Significant *CK* values are observed in the exit region of the Atlantic jet and both flanks of Asian jet (Fig. 5a). In the mid-latitude NA and the west of CA, *CK* values are positive; in the high-latitude NA and the east of CA, *CK* values are negative. The spatial characteristics of *CP* are manifested as alternating positive and negative values along the atmospheric wave train, with amplitudes of positive values being greater than negative ones (Fig. 5b). Overall, the contribution of *CP* exceeds that of *CK*. *CP* plays a major role in maintaining the wave

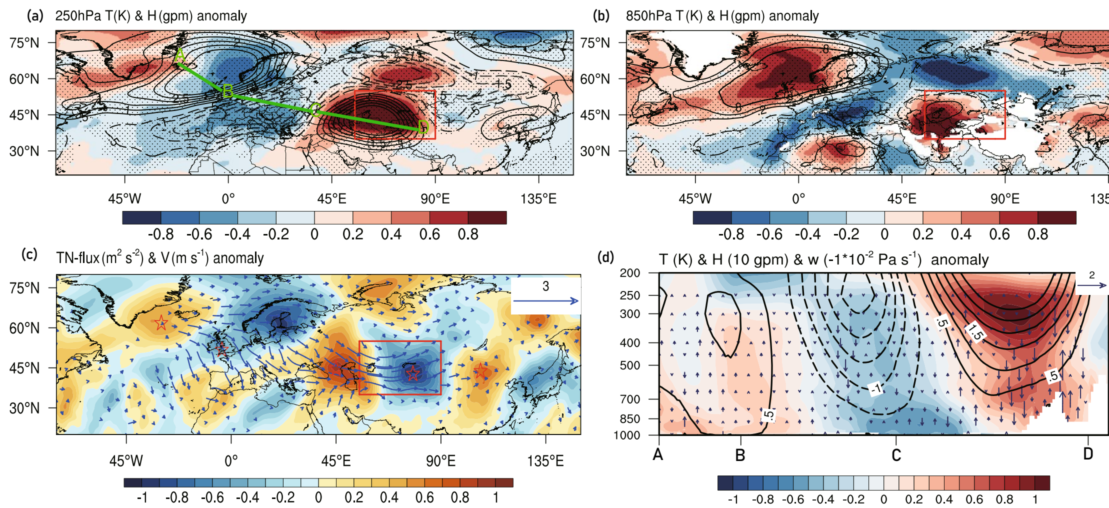

Fig. 2 Anomalies characteristics of the summer. **a** 250 hPa zonal deviation field of geopotential height (contour; units: gpm) and 250 hPa temperature (shading; K) during the drought periods. **b** Is the same as **a**, but for 850 hPa. The areas with dot markers indicate the differences exceed 95% significance level. **c** Composite 250 hPa wave activity fluxes (vectors, unit: m^2 s^{-2}) and meridional wind (shading; V) anomalies. Red boxes represent the CA region. The five major meridional wind action centers are labeled with red pentagram. **d** Vertical profile of the composite anomalies of the zonal deviation field of temperature (shading; T), geopotential height (contour; H) and vertical velocity (Arrow; ω) along the solid green line in (a)

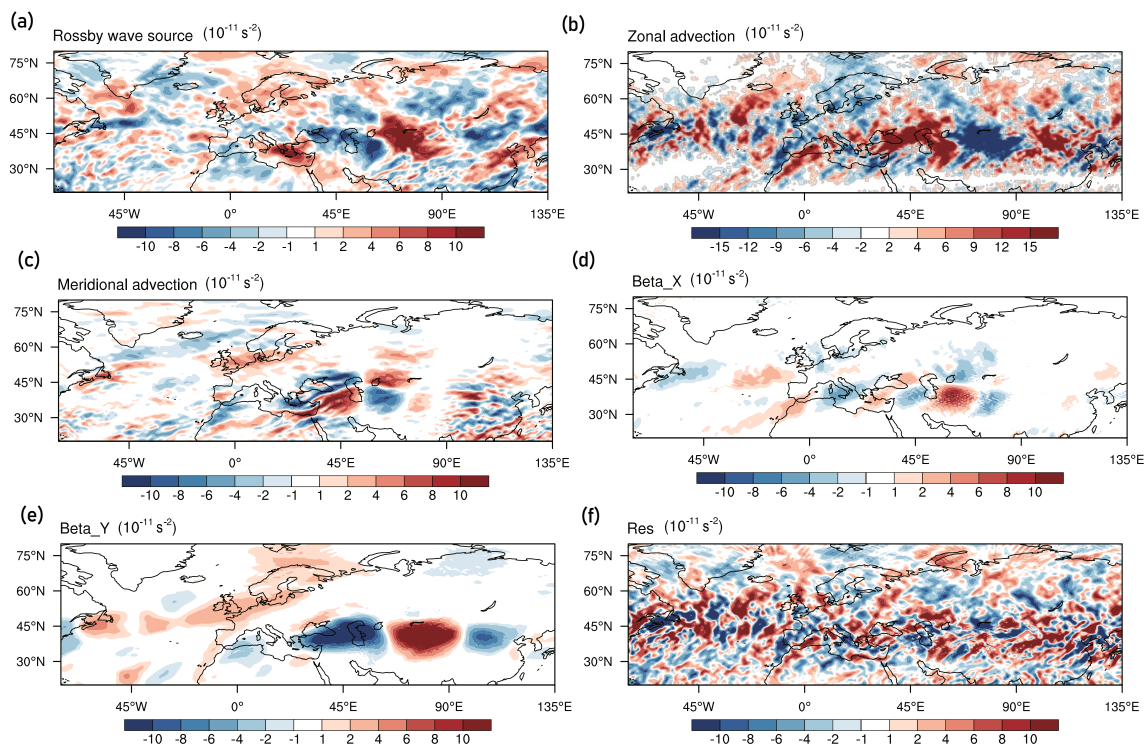

Fig. 3 Composite anomalies of vorticity budget of 250 hPa winds during drought periods. **a** The Rossby wave source term (*RWS*), **b** the zonal advection term (*ZA*), **c** the meridional advection term (*MA*), **d** the transport of mean vorticity by disturbed zonal rotating wind (β_x) term, **e** the transport of mean vorticity by disturbed meridional rotating wind (β_y) term and **f** the residuals. Unit: 10^{-11} s^{-2}

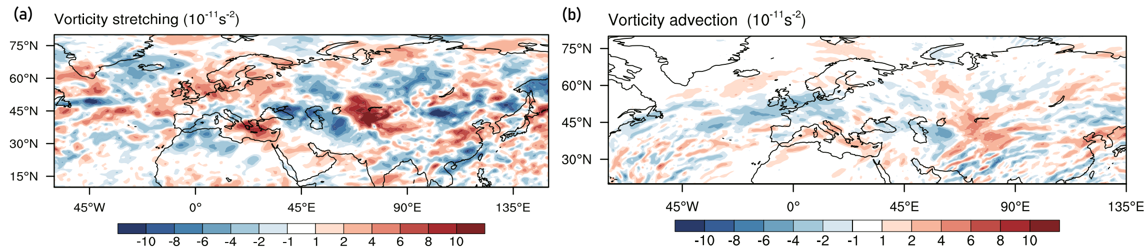

Fig. 4 Composite anomalies of **a** 250 hPa vortex stretching term and **b** absolute vorticity advection term during drought periods. Unit: 10^{-11} s^{-2}

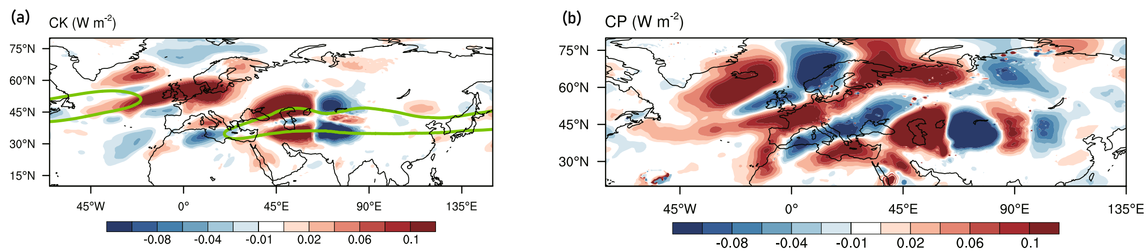

Fig. 5 Vertically integrated (from surface to 100 hPa) conversion of **a** kinetic energy and **b** available potential energy. Unit: W m^{-2}. The green contour line represent summer mean zonal wind speeds above 20 m s^{-1}

train, while *CK*'s influence is relatively limited, primarily acting to stabilize the positions of the wave train.

5 Local thermal mechanisms responsible for the CA drought

Atmospheric circulation anomalies play an essential role in modulating local heat fluxes by influencing radiation process and cloud cover (Horton et al. 2016; Liu and Sun 2023). Under the control of anomalous anticyclone of the middle to upper troposphere, CA experiences strong anomalous downward motion (Fig. 6a), which is most significantly in central and eastern CA. This subsidence is accompanied by a decrease in total cloud cover (Fig. 6b) and an increase in outgoing longwave radiation (Fig. 6c). Under such conditions, the downward longwave radiation at the surface decreases (Fig. 6e), allowing more shortwave radiation to penetrate the atmosphere and reach the ground (Fig. 6d). Additionally, the adiabatic warming effect of the subsidence further increases surface temperature in CA (Fig. 6g). With almost constant net radiation at the surface (Fig. 6f), enhanced sensible heat flux (Fig. 6h) and reduced latent heat flux (Fig. 6i) are more conducive to maintaining drought conditions.

The significant reduction in latent heat flux implies a marked decrease in evapotranspiration during the drought periods. Precipitation is composed of two components: one part originates from local evapotranspiration, referred to as "recycled precipitation (P_e)" and the other from the advection of external moisture, referred to as "advected precipitation (P_a)". The impact of local evapotranspiration on precipitation deficits merits further quantification. During the drought periods, total precipitation in CA decreases by 7.75 mm, of which P_e contributes 6.85 mm and P_a contributes 0.90 mm (Fig. 7b–d). This is accompanied by a significant decrease in the recycling ratio (Fig. 7a). The spatial patterns of the changes in P_e and total precipitation are also highly similar (Fig. 7b, c), indicating that the decrease in P_e caused by the decrease in evapotranspiration dominates the reduction in the total precipitation. We further gave the moisture contribution of the water vapor sources to the CA precipitation. Figure 8a shows the climatological mean moisture sources contributions to the CA summer rainfall, the sum of moisture tracked is 91.72%. The spatial extent of the sources covers the Eurasia continent, the North Atlantic, the Western Pacific, and the tropical Indian Ocean. During drought periods, there is primarily a relative reduction in moisture source contributions from CA (−4.32%), Western Europe (−11.69%), the North Atlantic (−8.85%), and the Indian Peninsula (−2.02%) (Fig. 8b, c); while moisture source contributions from the central-western and northern parts of the Eurasian continent increase (6.60 and 5.81%) (Fig. 8b, c), which is closely related to an anticyclonic anomaly over CA, enhancing water vapor transport from these regions along the west of anticyclone.

Furthermore, precipitable water significantly decreases (Fig. 9a). A detailed analysis of the atmospheric water budget over CA (Fig. 9b) reveals that there are minimal changes in the inflow (climatological mean: 44.53 kg m^{-1} s^{-1}; anomaly: 44.58 kg m^{-1} s^{-1}) and outflow (climatological mean:

53.25 kg m^{-1} s^{-1}; anomaly: 51.83 kg m^{-1} s^{-1}) of moisture flux to the region. This indicates that external moisture transport has little impact on maintaining drought. Instead, droughts are primarily influenced by local land–atmosphere interactions reducing local evapotranspiration (climatological mean: 24.86 kg m^{-1} s^{-1}; anomaly: 21.01 kg m^{-1} s^{-1}), with the circulation field providing a large-scale background conducive to drought.

6 Simulation for the modulation of North Atlantic

By the above-mentioned TN-wave activity fluxes and RWS analysis, we have demonstrated that the NA ocean may play a key role in exciting the eastward propagation Rossby wave by the diabatic heating or vorticity perturbation (Ghosh et al. 2017; Sheng et al. 2022), leading to the positive geopotential height anomalies over CA during the drought periods. The following provides a preliminary physical picture on how the NA SST affects CA precipitation variability. We first selected five 250 hPa anomalous meridional wind (V_*) activity centers from Fig. 2c, and defined an index reflecting wave train intensity as "*ZS5*", which formulation can be seen as follows:

$$
\begin{aligned}
ZS5 = 2/5[&V_*(62^\circ\mathrm{N}, 30^\circ\mathrm{W}) + V_*(45^\circ\mathrm{N}, 45^\circ\mathrm{E}) \\
&+ V_*(44^\circ\mathrm{N}, 107^\circ\mathrm{E})] - 3/5[V_*(52^\circ\,\mathrm{N}, 4^\circ\mathrm{W}) \\
&+ V_*(43^\circ\mathrm{N}, 78^\circ\mathrm{E})]
\end{aligned} \tag{13}
$$

The NA SST field and 250 hPa relative vorticity field is further regressed on *ZS5*. As can be seen in Fig. 10a, the significant positive SST anomalies over the mid-latitude eastern NA and negative SST anomalies over extratropical western NA can be observed, which is correspond well to the pronounced negative relative vorticity in the mid-latitude eastern NA (blue box: 50° N–58° N, 10° W–31° W) and marked positive relative vorticity in the extratropical western NA (red box: 58° N–67° N, 28° W–65° W) (Fig. 10b), although with somewhat lower significance in places for high-latitude SST anomalies. The middle and high latitude SST impacts atmosphere through the indirect dynamical and thermal forcing by atmospheric transient eddy activities (Fang and Yang 2016). The cooling of SST at high latitudes strengthens the meridional gradient of SST around 58° N, accompanied by an increase in the baroclinicity of the lower atmosphere, leading to more transient eddy activities. The transient eddy vorticity forcing induces a whole-layer negative geopotential tendency over the cold SST area, conducive to the low-pressure anomaly there (Chen et al. 2020; Song and Chen 2023). The vertical profiles of anomalous relative vorticity over the significant areas (red and blue boxes in Fig. 10b) during drought periods are shown in Fig. 10c, where the peak of vorticity is distributed at 300 hPa. To further validate vorticity perturbations can excite the eastward-propagating Rossby wave, a numerical experiment to simulate the atmospheric response to vorticity forcing over NA based on LBM is conducted, and the vertical profiles of Fig. 10c is used to force the experiment. The model response of the geopotential height and meridional wind at 250 hPa to the above vorticity forcing is depicted in Fig. 11 from day 30 to day 60. A series of alternating positive and negative height anomalies are observed over Eurasia, forming a wave train-like pattern extending from the NA Ocean to the East Asia, with an anomalous anticyclone over CA (Fig. 11a, b). The results of the numerical experiment show a structure similar to that of the composite circulation pattern (Fig. 2a, c). Thus, the anomalous SST and its related vorticity in the mid-high latitude NA can be considered a trigger factor for the drought over CA.

7 Conclusion and discussion

In this study, we focused on the summer drought of CA and explored its underlying physical mechanism using MERRA-2 reanalysis data. All processes are summarized in Fig. 12. First, for the large-scale circulation, composite analysis show that the CA drought is closely associated with a high-pressure anomaly over CA. This anomaly is related to a large-scale extratropical anomalous wave train from the high-latitude NA to East Asia, featuring positive anomaly centers in extratropical NA and CA, and negative anomalous centers in the Europe and western Russia. The anomalous wave energy propagates from the extratropical western NA toward East Asia. Meanwhile, significant negative SST anomalies appear in the high-latitude western NA and positive SST anomalies occur in the mid-latitude eastern NA during summer. This pattern corresponds to positive vorticity anomalies in the former and negative vorticity anomalies in the latter. These results suggest that on the interannual scale, the anomalous wave train is associated with the variation of mid-high latitudes SST in the NA. The LBM model experiments further verify the impact of the NA vorticity anomalies.

Meanwhile, under the control of anticyclone, significant subsidence occurs in CA, accompanied by anomalously low cloud cover. This results in increased OLR, enhanced downward shortwave radiation at the surface, and reduced downward longwave radiation. The net radiation at the surface has little change, leading to an increase in sensible heat and a decrease in latent heat flux (Fig. 12). The reduction in latent heat implies a decrease in actual evapotranspiration. By using the DRM model, we further quantified the role of the decrease in local evapotranspiration on the drought.

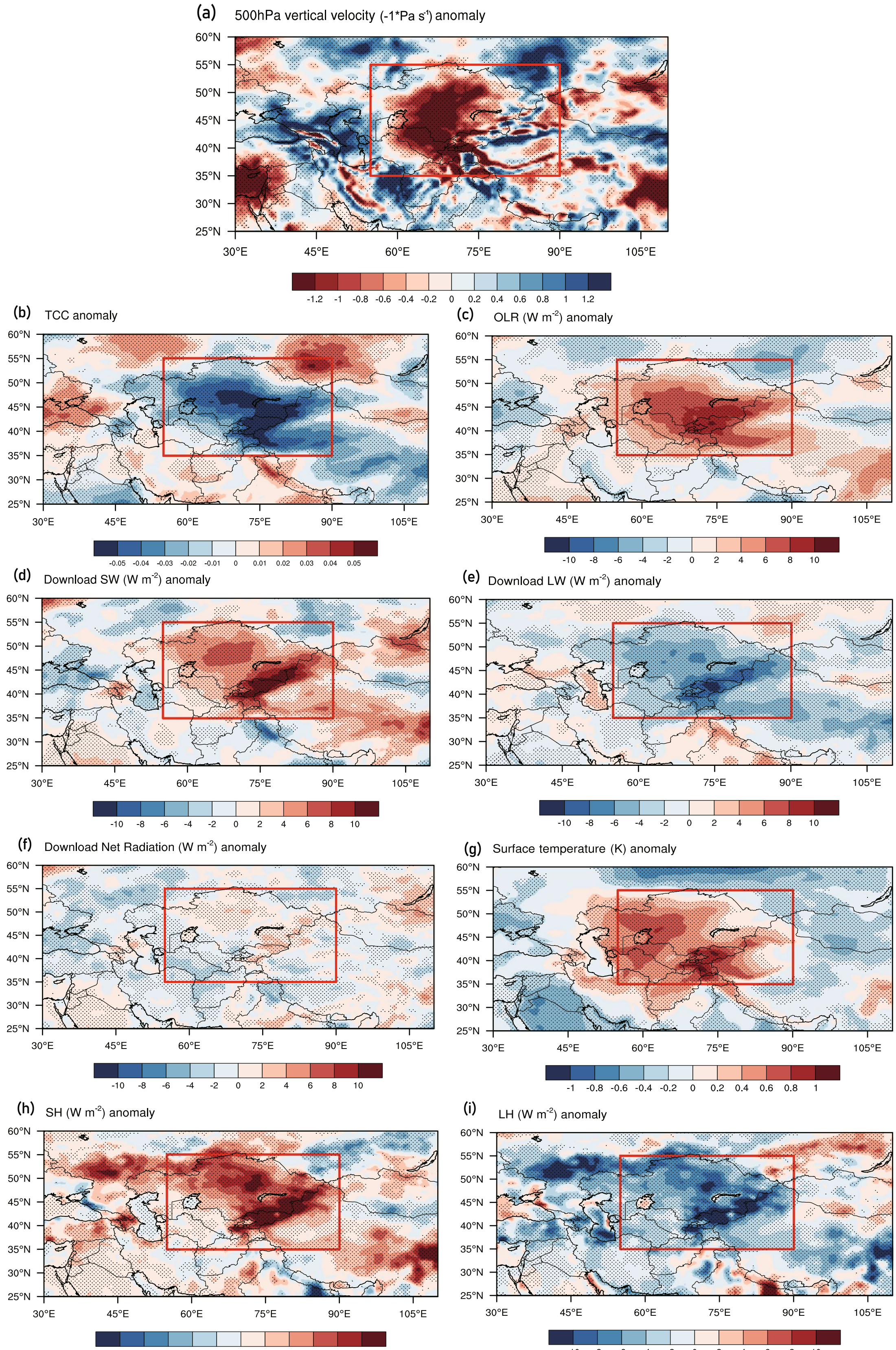
(a) 500hPa vertical velocity (-1*Pa s-1) anomaly
60°N 55°N 50°N 45°N 40°N 35°N 30°N 25°N
30°E 45°E 60°E 75°E 90°E 105°E
-1.2 -1 -0.8 -0.6 -0.4 -0.2 0 0.2 0.4 0.6 0.8 1 1.2
(b) TCC anomaly
-0.05 -0.04 -0.03 -0.02 -0.01 0 0.01 0.02 0.03 0.04 0.05
(c) OLR (W m-2) anomaly
-10 -8 -6 -4 -2 0 2 4 6 8 10
(d) Download SW (W m-2) anomaly
(e) Download LW (W m-2) anomaly
(f) Download Net Radiation (W m-2) anomaly
(g) Surface temperature (K) anomaly
-1 -0.8 -0.6 -0.4 -0.2 0 0.2 0.4 0.6 0.8 1
(h) SH (W m-2) anomaly
(i) LH (W m-2) anomaly

◂**Fig. 6** Anomalies of the **a** 500 hPa vertical velocity (-1^{*}Pa s^{-1}), **b** total cloud cover, **c** outgoing longwave radiation (W m^{-2}), **d** surface downward shortwave radiation (W m^{-2}), **e** surface downward longwave radiation (W m^{-2}), **f** surface downward net radiation (W m^{-2}), **g** surface temperature (K), **h** sensible heat flux (W m^{-2}) and **i** latent heat flux (W m^{-2}) during drought period. The dotted grid represents anomalies significant at the 95% confidence level

The recycled precipitation, induced by the local evapotranspiration, contributes to 88.39% of the decrease in total precipitation during the drought periods. Further quantifying the moisture contributions from source regions, the total moisture tracked in the climatological state amounts to 91.72% for CA precipitation. For drought periods, negative moisture contribution anomalies are concentrated in CA, the Indian Peninsula, Western Europe, and the North Atlantic Ocean. Conversely, water vapor contributions from the western and northern parts of Eurasia have increased, which is closely related to the circulation patterns. We finally gave the moisture balance for CA and found that compared to the climatology, the inflow of external advected moisture did not significantly decrease during drought periods. Instead, a marked reduction in local evapotranspiration, triggered by local thermal forcing, is the primary factor sustaining the drought conditions, and anomalies in large-scale circulation provides a favorable background for the drought.

For the Atlantic SST, it changes are closely linked to the North Atlantic Oscillation (NAO) variations in recent decades. The NAO significantly modulated interannual variability of drought (measured by SPEI) and summer temperature across most subregions of CA (De Beurs et al. 2018; Guo et al. 2018). The anomalously negative NAO modulates the partitioning of latent and sensible heat, thereby playing a contributing role in the heat wave observed over the northern parts of CA (Wright et al. 2014). In contrast, under a positive NAO pattern coupled with a cyclone over CA, the northeastern regions of CA exhibit a positive precipitation anomaly (Hua et al. 2017a, b). Particularly during positive phases of the Summer North Atlantic Oscillation (SNAO), on one hand, the North Atlantic storm track shifts northward, enhancing tropospheric transient eddy activity. This activity propagates eastward through CA and Mongolia, increasing precipitation in northeastern Eurasia; on the other hand, the quasi-stationary wave originating from the NAO center extends eastward across the Eurasian Continent (Linderholm et al. 2011; Sun and Wang 2012). Additionally, the relationship between the AMO and the SNAO

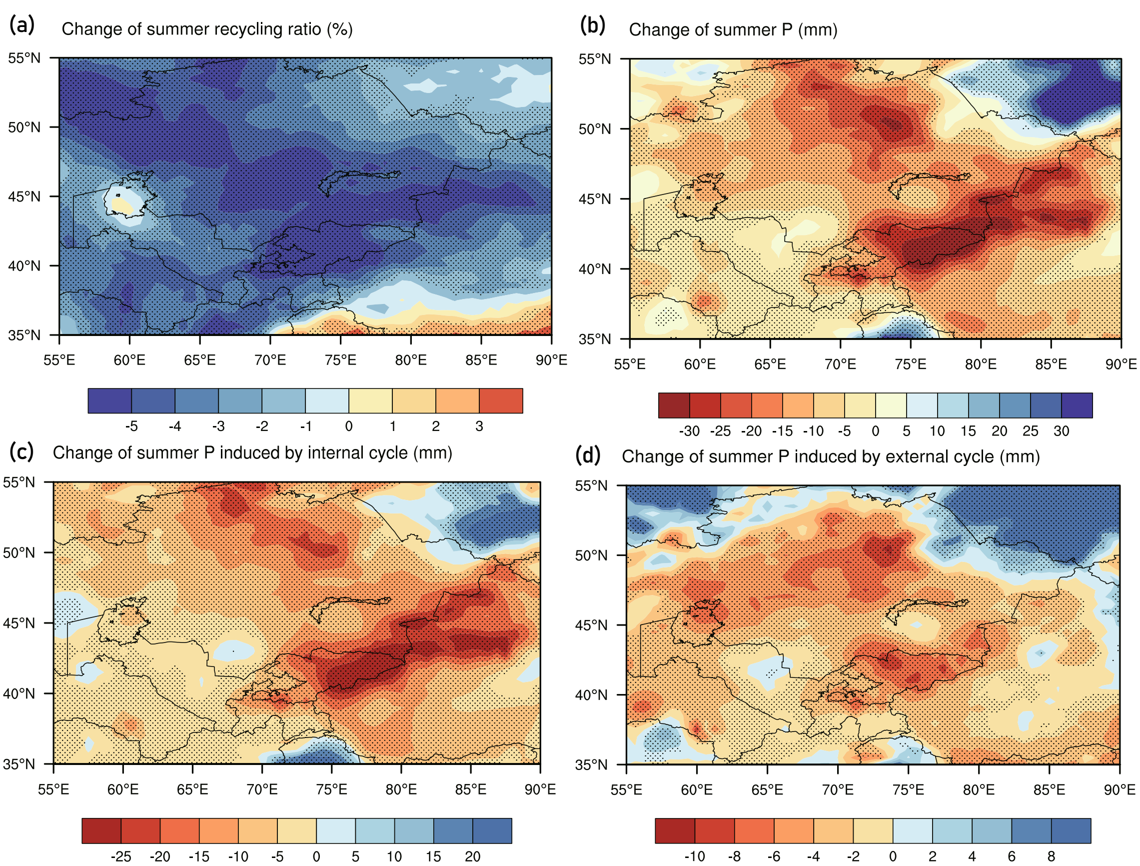

Fig. 7 Spatial patterns of anomalies of **a** recycling ratio (%), **b** total precipitation (mm), **c** precipitation induced by internal cycle (mm), and **d** precipitation induced by external cycle (mm) during drought periods over CA. The dotted regions represent anomalies significant at the 95% confidence level

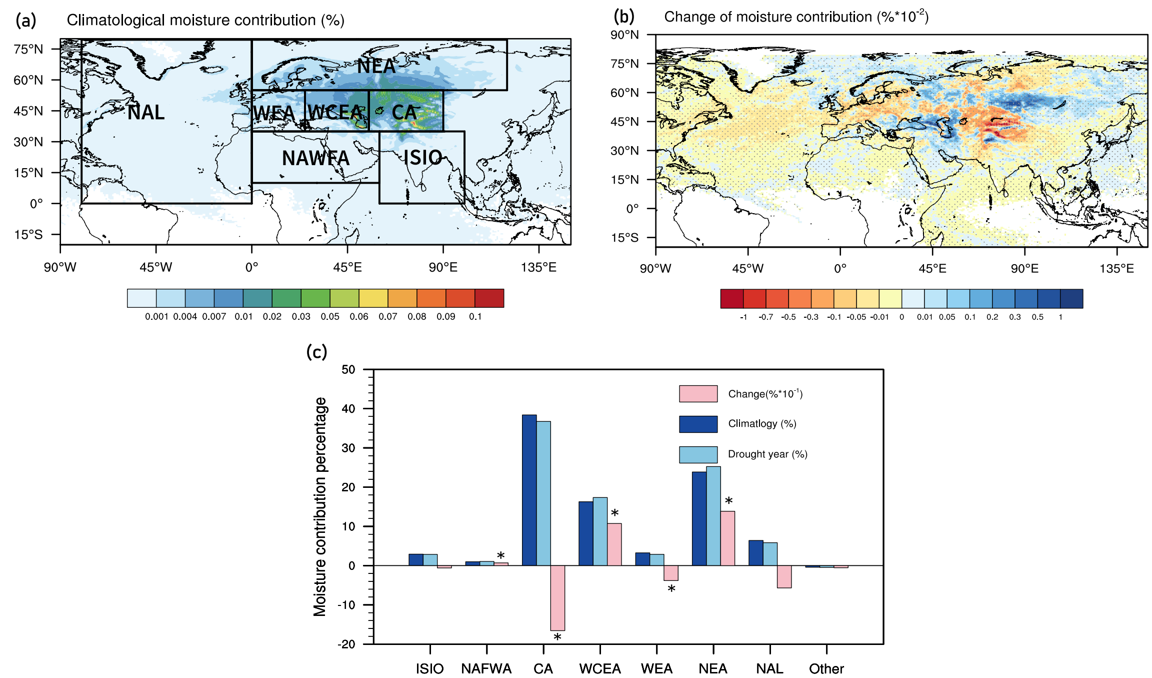

Fig. 8 **a** The spatial patterns of the climatological summer mean moisture contribution (%). **b** The differences in moisture contribution between the drought periods and the climatology means. The dotted regions indicate anomalies significant at the 95% confidence level. **c** The spatiotemporal average moisture contributions for the climatological mean (blue bar), drought years (skyblue bar) and the difference between them (pink bar). The * represents that the difference is significant at the 0.05 level. The black boxes in **a** represent the defined geographic regions: the North Atlantic Ocean (NAL: 0° N–80° N, 80° W–0° E), Northern Eurasia (NEA: 55° N–80° N, 0° E–120° E), Western Eurasia (WEA: 35° N–55° N, 0° E–25° E), Midwestern Eurasia (WCEA: 35° N–55° N, 25° E–55° E), Central Asia (CA: 35° N–55° N, 55° E–90° E), North Africa and West Asia (NAFWA: 10° N–35° N, 0° E–60° E), and the Indian subcontinent and the Indian Ocean (ISIO: 0° N–35° N, 60° E–100° E)

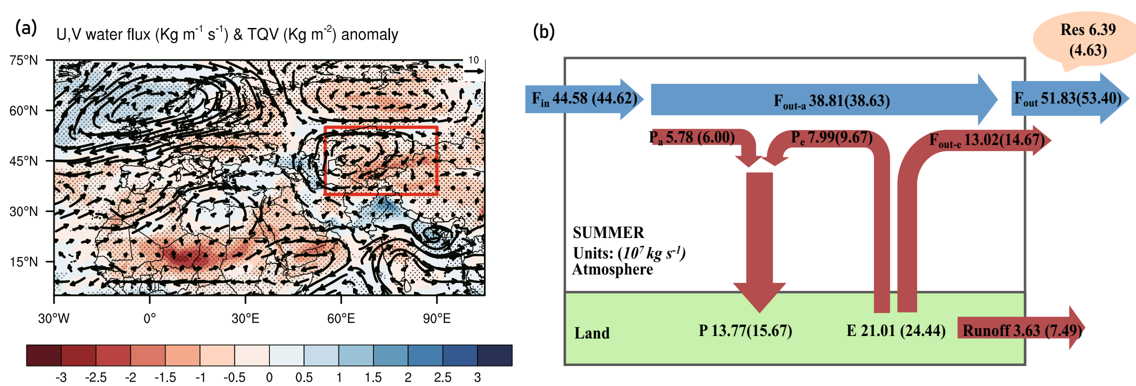

Fig. 9 **a** Anomaly in vertical integrated water vapor flux (vector; kg m^{-1} s^{-1}) and precipitable water (shades; Kg m^{-2}) during drought periods relative to the climatological mean. **b** Schematic diagrams of the land–atmosphere water balance for the climatological mean (in black brackets) and the drought periods. The variables in this figure include horizontal external advected moisture inflow (F_{in}), the precipitation caused by the external moisture advection (P_a), the precipitation caused by the local evaporation (P_e), local evapotranspiration (E), the advected moisture flows out of this region ($F_{out\text{-}a}$), the outflowing water vapor produced by the local evapotranspiration ($F_{out\text{-}e}$), runoff and horizontal moisture outflow the region (F_{out})

over periods exceeding 10 years reveals that a cold (warm) phase of the AMO corresponds to a positive (negative) phase of the SNAO (Sutton and Dong 2012). Consequently, the indirect impact of the AMO warrants further consideration. Additional factors such as the Arctic ice, Tibetan Plateau snow cover, aerosols, greenhouse gases, and others should also be evaluated for their potential influence on CA drought.

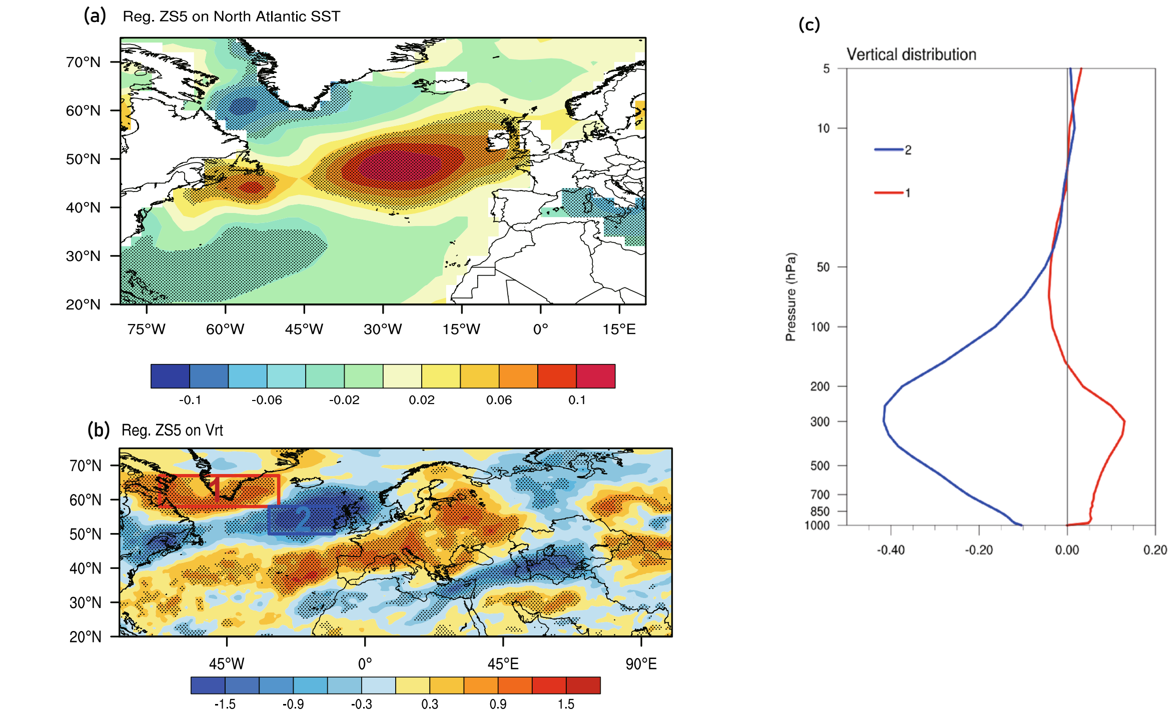

Fig. 10 Selection of the LBM vorticity sensitivity test. The **a** North Atlantic SST and **b** 250 hPa vorticity regressed to *ZS5* index (the two significant areas are defined as the "1" and "2" areas). The dotted regions indicate regression significant at the 95% confidence level. **c** Vertical profiles of the averaged vorticity anomalies over significant areas in **b** during drought periods

Although our results provide a detailed elucidation of the primary circulation systems that sustain drought and quantify the associated moisture transport anomalies, this study still has some limitations, which are outlined below. Firstly, DRM is a 'analytical' model that employs simple budget equations to quantify sources and sinks of precipitation. It does not account for all the physical processes that influence atmospheric moisture, such as advection, convection, and cloud microphysics. Additionally, the LBM model used in this study has a relatively low resolution (T42) and a simplified structure, which may not fully capture the complex air-sea interactions. To gain a more comprehensive understanding of the physical mechanisms through which North Atlantic SST anomalies influence CA drought, experiments using coupled ocean–atmosphere models could be advantageous. Unlike atmospheric models, coupled models can simulate both the atmospheric response and the air-sea feedbacks under SST forcing in the specific area. Such models could provide more accurate verification and offer valuable insights for future research. Furthermore, the use of a reanalysis dataset is primarily motivated by its ability to depict coupled land–atmosphere interactions and quantify multiple fluxes and processes, which is not achievable with observational data alone. However, reanalysis product also has its data bias. Therefore, observation-based investigations would be the most direct approach for verifying the findings of this study.

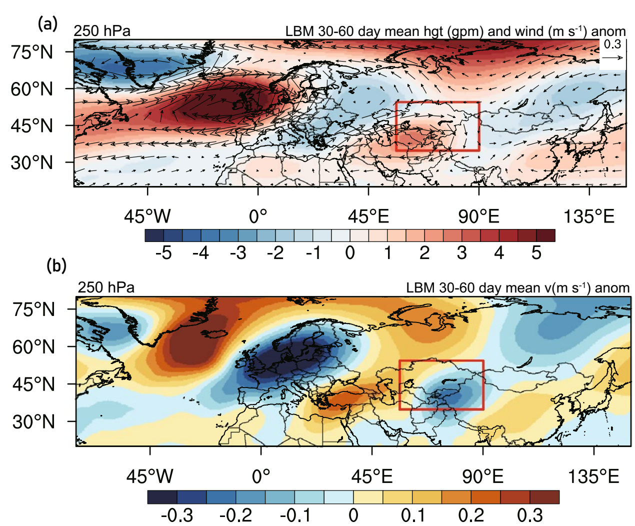

Fig. 11 Spatial distribution of **a** the 250 hPa geopotential height (shaded; gpm) and wind field (vector; m s^{-1}) and **b** 250 hPa meridional wind (m s^{-1}) under the vorticity forcing in the LBM experiment

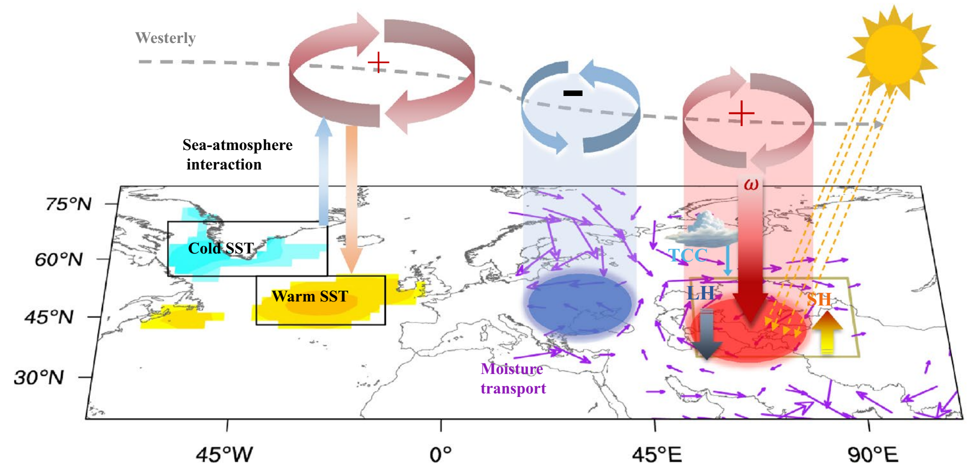

Fig. 12 A schematic diagram of the mechanism responsible for the drought in CA. TCC, SH and LH represent the total cloud cover, sensible heat flux, and the latent heat flux, respectively. The ω is the subsidence. The purple arrows are the vertically integrated moisture flux anomaly

Author contributions HY and JH contributed to the concept and design of the research. YR conducted the analysis and prepared the draft. All authors analyzed and discussed the results, commented on the manuscript, and contributed to the manuscript.

Funding This work was supported by the National Natural Science Foundation of China (41991231, 42122034, 42075043), the Youth Innovation Promotion Association of Chinese Academy of Sciences (2021427), Key talent project in Gansu and Central Guidance Fund for Local Science and Technology Development Projects in Gansu (No.24ZYQA031).

Data availability The SPEI-3 data are downloaded from https://spei.csic.es/spei_database/#map_name=spei03%23map_position=1459. The MERRA-2 reanalysis data are derived from https://disc.gsfc.nasa.gov/datasets?project=MERRA-2. The ERSST data are available at https://www.ncei.noaa.gov/products/extended-reconstructed-sst.

Declarations

Conflict of interest The authors have no relevant financial or non-financial interests to disclose.

Ethics approval and consent to participate Not applicable.

Consent for publication Not applicable.

References

Bestelmeyer BT, Okin GS, Duniway MC et al (2015) Desertification, land use, and the transformation of global drylands. Front Ecol Environ 13(1):28–36
Bothe O, Fraedrich K, Zhu X (2012) Precipitation climate of Central Asia and the large-scale atmospheric circulation. Theoret Appl Climatol 108:345–354
Chen Y, Li W, Deng H, Fang G, Li Z (2016) Changes in Central Asia's water tower: past, present and future. Sci Rep 6(1):35458
Chen L, Fang J, Yang XQ (2020) Midlatitude unstable air-sea interaction with atmospheric transient eddy dynamical forcing in an analytical coupled model. Clim Dyn 55(9):2557–2577
De Beurs KM, Henebr GM, Owsley BC, Sokolik IN (2018) Large scale climate oscillation impacts on temperature, precipitation and land surface phenology in Central Asia. Environ Res Lett 13(6):065018
Dominguez F, Kumar P (2008) Precipitation recycling variability and ecoclimatological stability—a study using NARR data. Part I: Central US plains ecoregion. J Clim 21(20):5165–5186
Dominguez F, Kumar P, Liang XZ, Ting M (2006) Impact of atmospheric moisture storage on precipitation recycling. J Clim 19:1513–1530. https://doi.org/10.1175/jcli3691.1
Fang J, Yang XQ (2016) Structure and dynamics of decadal anomalies in the wintertime midlatitude North Pacific ocean–atmosphere system. Clim Dyn 47:1989–2007
Gelaro R, McCarty W, Suárez MJ et al (2017) The modern-era retrospective analysis for research and applications, version 2 (MERRA-2). J Clim 30(14):5419–5454
Ghosh R, Müller WA, Baehr J et al (2017) Impact of observed North Atlantic multidecadal variations to European summer climate: a linear baroclinic response to surface heating. Clim Dyn 48:3547–3563
Guan Y, Gu X, Slater LJ et al (2022) Tracing anomalies in moisture recycling and transport to two record-breaking droughts over the Mid-to-Lower Reaches of the Yangtze River. J Hydrol 609:127787
Guo H, Bao A, Liu T et al (2018) Spatial and temporal characteristics of droughts in Central Asia during 1966–2015. Sci Total Environ 624:1523–1538
Guo S, Guan X, Gao L et al (2022) Opposite Atlantic Multidecadal Oscillation effects on dry/wet changes over Central and East Asian drylands. Atmos Res 271:106102
Heim RR (2002) A review of twentieth-century drought indices used in the United States. Bull Am Meteorol Soc 83(8):1149–1166
Horton RM, Mankin JS, Lesk C, Coffel E, Raymond C (2016) A review of recent advances in research on extreme heat events. Curr Clim Change Rep 2:242–259
Hu Z, Zhou Q, Chen X et al (2017) Variations and changes of annual precipitation in Central Asia over the last century. Int J Climatol 37(S1):157–170
Hua L, Zhong L, Ma Z (2017a) Decadal transition of moisture sources and transport in northwestern China during summer from 1982 to 2010. J Geophys Res Atmos 122(23):12–522
Hua L, Zhong L, Ke Z (2017b) Characteristics of the precipitation recycling ratio and its relationship with regional precipitation in China. Theoret Appl Climatol 127:513–531
Huang J, Li Y, Fu C (2017) Dryland climate change: Recent progress and challenges. Rev Geophys 55(3):719–778

IPCC (2021) Summary for policymakers. In: Masson-Delmotte V, Zhai P, Pirani A, Connors SL, Péan C, Berger S, Caud N, Chen Y, Goldfarb L, Gomis MI, Huang M, Leitzell K, Lonnoy E, Matthews JBR, Maycock TK, Waterfield T, Yelekçi O, Yu R, Zhou B (eds) Climate change 2021: the physical science basis. Contribution of working group I to the sixth assessment report of the intergovernmental panel on climate change. Cambridge University Press, Cambridge, United Kingdom and New York, NY, USA, pp 3–32, https://doi.org/10.1017/9781009157896.001

Ji F, Wu Z, Huang J (2014) Evolution of land surface air temperature trend. Nat Clim Chang 4(6):462–466

Jiang J, Zhou T (2021) Human-induced rainfall reduction in drought-prone northern central Asia. Geophys Res Lett 48(7):e2020GL092156

Jiang J, Zhou T (2023) Agricultural drought over water-scarce Central Asia aggravated by internal climate variability. Nat Geosci 16(2):154–161

Jiang J, Zhou T, Wang H et al (2020) Tracking moisture sources of precipitation over central Asia: a study based on the water-source-tagging method. J Clim 33(23):10339–10355

Kosaka Y, Nakamura H (2006) Structure and dynamics of the summertime Pacific-Japan teleconnection pattern. Quart J Roy Meteorol Soc J Atmos Sci Appl Meteorol Phys Oceanogr 132(619):2009–2030

Kumar KN, Rajeevan M, Pai DS et al (2013) On the observed variability of monsoon droughts over India. Weather Clim Extremes 1:42–50

Li Z, Chen Y, Li W, Deng H, Fang G (2015) Potential impacts of climate change on vegetation dynamics in Central Asia. J Geophys Res Atmos 120(24):12345–12356

Li Z, Chen Y, Fang G, Li Y (2017) Multivariate assessment and attribution of droughts in Central Asia. Sci Rep 7(1):1316

Linderholm HW, Ou T, Jeong JH, Folland CK, Gong D, Liu H, Liu Y, Chen D (2011) Interannual teleconnections between the summer North Atlantic Oscillation and the East Asian summer monsoon. J Geophys Res 116:D13107. https://doi.org/10.1029/2010JD015235

Liu S, Sun J (2023) Enhanced influence of tropical Pacific sea surface temperature anomalies on spring extreme heat events over mid-high latitude Eurasia. J Geophys Res Atmos 128(12):e2022JD037837

Lorenz EN (1956) Empirical orthogonal functions and statistical weather prediction. Massachusetts Institute of Technology, Department of Meteorology, Cambridge, vol 1, p 52

Lu R, Kim BJ (2004) The climatological Rossby wave source over the STCZs in the summer Northern Hemisphere. J Meteorol Soc Jpn Ser II 82(2):657–669

Ma Q, Zhang J, Game AT, Chang Y, Li S (2020) Spatiotemporal variability of summer precipitation and precipitation extremes and associated large-scale mechanisms in Central Asia during 1979–2018. J Hydrol X 8:100061

McKee TB, Doesken NJ, Kleist J (1995) Drought monitoring with multiple time scales. In: American Meteorological Society: ninth conference on applied climatology, pp 233–236

Meng L, Zhao Y, Li M (2021) Effects of whole SST anomaly in the tropical Indian Ocean on summer rainfall over Central Asia. Front Earth Sci 9:738066

Mishra AK, Singh VP (2010) A review of drought concepts. J Hydrol 391(1–2):202–216

Mukherjee S, Mishra A, Trenberth KE (2018) Climate change and drought: a perspective on drought indices. Curr Clim Change Rep 4:145–163

Palmer WC (1965) Meteorological drought. U.S. Research Paper No.45. Department of Commerce Weather Bureau

Pathak A, Ghosh S, Kumar P (2014) Precipitation recycling in the Indian subcontinent during summer monsoon. J Hydrometeorol 15(5):2050–2066

Peng D, Zhou T, Zhang L, Zou L (2019) Detecting human influence on the temperature changes in Central Asia. Clim Dyn 53:4553–4568

Peng D, Zhou T, Zhang L (2020) Moisture sources associated with precipitation during dry and wet seasons over Central Asia. J Clim 33:10755–10771

Portela MM, dos Santos JF, Silva AT (2015) Drought analysis in southern Paraguay, Brazil and northern Argentina: regionalization, occurrence rate and rainfall thresholds. Hydrol Res 46(5):792–810

Ren G, Zhao Y (2023) Decadal variability of the subtropical westerly jet and its association with circulation and rainfall over Central Asia. Clim Environ Res (in Chinese) 28(4):356–366

Ren Y, Yu H, Liu C et al (2022) Attribution of dry and wet climatic changes over Central Asia. J Clim 35(5):1399–1421

Roy T, Martinez JA, Herrera-Estrada JE et al (2019) Role of moisture transport and recycling in characterizing droughts: perspectives from two recent US droughts and the CFSv2 system. J Hydrometeorol 20(1):139–154

Sardeshmukh PD, Hoskins BJ (1988) The generation of global rotational flow by steady idealized tropical divergence. J Atmos Sci 45(7):1228–1251

Sheng C, He B, Wu G et al (2022) Interannual impact of the North Atlantic tripole SST mode on the surface potential vorticity over the Tibetan Plateau during boreal summer. J Geophys Res Atmos 127(9):e2021JD036369

Sodemann H, Schwierz C, Wernli H (2008) Interannual variability of Greenland winter precipitation sources: Lagrangian moisture diagnostic and North Atlantic Oscillation influence. J Geophys Res 113:D03107. https://doi.org/10.1029/2007JD008503

Song Y, Chen H (2023) Influence of the late-winter North Atlantic Tripole Sea surface temperature anomalies on spring land surface temperature in mid-to-high latitudes of Western Eurasia. J Clim 36(15):4933–4950

Sun J, Wang H (2012) Changes of the connection between the summer North Atlantic Oscillation and the East Asian summer rainfall. J Geophys Res Atmos 117:D08110. https://doi.org/10.1029/2012JD017482

Sutton RT, Dong B (2012) Atlantic Ocean influence on a shift in European climate in the 1990s. Nat Geosci 5(11):788–792

Vicente-Serrano SM, Beguería S, López-Moreno JI et al (2010) A multiscalar drought index sensitive to global warming: the standardized precipitation evapotranspiration index. J Clim 23(7):1696–1718

Watanabe M, Kimoto M (2000) Atmosphere-ocean thermal coupling in the North Atlantic: a positive feedback. Q J R Meteorol Soc 126(570):3343–3369

Wright CK, De Beurs KM, Henebry GM (2014) Land surface anomalies preceding the 2010 Russian heat wave and a link to the North Atlantic oscillation. Environ Res Lett 9(12):124015

Wei Y, Yu H, Li S, Zhu Z, Yang Y, Ren Y, Liu C, Zhou J (2023) Impact of North Indian atmospheric diabatic heating on summer precipitation in Central Asia. J Clim 36(13):4345–4362

Zhang G, Biradar CM, Xiao X et al (2018) Exacerbated grassland degradation and desertification in Central Asia during 2000–2014. Ecol Appl 28(2):442–456

Zhang J, Wang S, He Y et al (2022) Contribution of the precipitation-recycling process to the wetting trend in Xinjiang, China. J Geophys Res Atmos 127:e2021JD036407

Zhao S, Zhang J, Du Y et al (2022) Modulation of coupled modes of Tibetan Plateau heating and Indian summer monsoon on summer rainfall over central Asia. J Clim 35(5):1441–1458

Zhao Z, Hao X, Fan X et al (2023) Actual evapotranspiration dominates drought in Central Asia. Remote Sens 15(18):4557

Zhou J, Yu H, Xu P et al (2024) Extreme heat event over Northwest China driven by Silk Road Pattern teleconnection and its possible mechanism. Atmos Res 297:107090

Publisher's Note Springer Nature remains neutral with regard to jurisdictional claims in published maps and institutional affiliations.